



HAL
open science

A Comparative IRMPD and DFT Study of Fe 3+ and UO 2 2+ Complexation with N -Methylacetohydroxamic Acid

Thibault Terencio, Jana Roithová, Stéphane Brandès, Yoann Rousselin,
Marie-José Penouilh, Michel Meyer

► **To cite this version:**

Thibault Terencio, Jana Roithová, Stéphane Brandès, Yoann Rousselin, Marie-José Penouilh, et al. A Comparative IRMPD and DFT Study of Fe 3+ and UO 2 2+ Complexation with N -Methylacetohydroxamic Acid. *Inorganic Chemistry*, 2018, 57 (3), pp.1125 - 1135. 10.1021/acs.inorgchem.7b02567 . hal-01857041

HAL Id: hal-01857041

<https://u-bourgogne.hal.science/hal-01857041>

Submitted on 20 Dec 2021

HAL is a multi-disciplinary open access archive for the deposit and dissemination of scientific research documents, whether they are published or not. The documents may come from teaching and research institutions in France or abroad, or from public or private research centers.

L'archive ouverte pluridisciplinaire **HAL**, est destinée au dépôt et à la diffusion de documents scientifiques de niveau recherche, publiés ou non, émanant des établissements d'enseignement et de recherche français ou étrangers, des laboratoires publics ou privés.

A Comparative IRMPD and DFT Study of Fe³⁺ and UO₂²⁺ Complexation with N-Methylacetohydroxamic Acid

Thibault Terencio,[†] Jana Roithová,^{*,†} Stéphane Brandès,[‡] Yoann Rousselin,[‡]

Marie-José Penouilh,[‡] and Michel Meyer^{*,‡}

[†] Department of Organic Chemistry, Faculty of Science, Charles University in Prague,
Hlavova 8, 128 43 Prague 2, Czech Republic

[‡] Institut de Chimie Moléculaire de l'Université de Bourgogne (ICMUB), UMR 6302, CNRS,
Université de Bourgogne–Franche-Comté, 9 avenue Alain Savary, BP 47870, 21078 Dijon
Cedex, France

Published on January 16, 2018 as an article in

Inorganic Chemistry **2018**, *57*, 1125–1135

DOI: 10.1021/acs.inorgchem.7b02567

* Corresponding author.

ABSTRACT

Iron(III) and uranyl complexes of *N*-methylacetohydroxamic acid (NMAH) have been investigated by mass spectrometry, infrared multiphoton dissociation (IRMPD) spectroscopy, and density functional theory (DFT) calculations. Comparison between IRMPD and theoretical IR spectra enabled to probe the structures for some selected complexes detected in the gas phase. The results show that the coordination of Fe³⁺ and UO₂²⁺ by the hydroxamic acid is of a very similar nature. Natural Bond Orbitals (NBO) analysis suggests that the bonding in the uranyl complexes possesses a slightly stronger ionic character than in the iron complexes. Collision induced dissociation (CID), IRMPD, and ¹⁸O-labelling experiments unambiguously revealed a rare example of the U=O bond activation concomitant with elimination of a water molecule from the gaseous [UO₂(NMA)(NMAH)₂]⁺ complex. The U=O bond activation is observed only for complexes with one monodentate NMAH molecule forming a hydrogen bond towards one "yl" oxygen atom, as found by DFT calculations. This reactivity might explain oxygen exchange observed for uranyl complexes.

Keywords: hydroxamate, siderophore, DFT, IRMPD spectroscopy, uranyl, iron

INTRODUCTION

Hydroxamic acids with a general formula $R^1C(=O)N(OH)R^2$ were first reported in 1869 by Lossen.¹ They are usually classified as primary if $R^2 = H$ or as secondary if R^2 is an alkyl or aryl group. Among the primary hydroxamic acids, formo- ($R^1 = R^2 = H$) and acetohydroxamic acids ($R^1 = CH_3$, $R^2 = H$) are the most studied ones. They exist as a mixture of different conformers (*Z* or *E*) and tautomers (H-migration).² Tautomerism involves the nitrogen-bound hydrogen atom, which can migrate to the carbonyl oxygen atom. This rearrangement can be prevented if an alkyl or aryl group is introduced to the nitrogen atom instead of the hydrogen atom. As the simplest representative of the secondary hydroxamic acids, we are focusing herein on *N*-methylacetohydroxamic acid (NMAH, $R^1 = R^2 = Me$), which prevails in the *E* form in aqueous solutions regardless of its protonation state.³

Hydroxamic acid moieties are present in a large number of siderophores. Their high affinity for iron(III) makes them particularly suitable for biological applications, and they are key compounds involved in Fe(III) transporting.⁴ It was shown that siderophores can also bind to other metal ions,⁵ thus highlighting their advantage in solving environmental issues such as water pollution by heavy metals.⁶ Most scientific effort was devoted until now to acetohydroxamic acid binding to transition metals. It was shown that this ligand, after deprotonation, acts as a bidentate ligand through its two oxygen atoms. Hydroxamates are strong oxodonor groups which can form stable complexes with hard Lewis acids.⁷ We and others have shown that coordination of the primary hydroxamates to alkali-metal ions can lead to their Lossen rearrangement and therefore to their degradation, provided that sufficient activation energy is supplied (i.e. heating to about 90 °C).^{5c,8} The rearrangement is associated with the migration of the hydrogen atom from the nitrogen to the terminal oxygen atom.⁹ The harder the metal ion is, the more is this rearrangement favored.

Actinides are known to establish strong bonds with oxygen atoms, thus, it has been suggested that siderophores can favorably bind to actinides.¹⁰ Among actinides, uranium is particularly wide-spread because of its use in nuclear industry. Uranium can also contaminate sea water, soils, or rivers from abandoned mines.¹¹ Related to this problem, complexation of uranium by hydroxamic acids gained increasing interest in order to separate uranium, from neptunium and plutonium, during treatment of nuclear fuel.¹²

While complexation of transition metals with hydroxamates was quite extensively studied,^{5b,13} structural and physico-chemical properties of the uranium complexes with hydroxamates are still not fully understood.^{12a,14} Recently, we described the first crystal structures of two mono- and bischelated uranyl (UO_2^{2+}) complexes incorporating the NMA^- ligand, having $[\text{UO}_2(\text{NMA})(\text{NO}_3)(\text{H}_2\text{O})_2]$ and $[\text{UO}_2(\text{NMA})_2(\text{H}_2\text{O})]$ compositions.³ The uranyl cations in these complexes are typically surrounded by five oxygen atoms located in the essentially flat equatorial plane, ruling out steric interactions between the bidentate NMA^- and the monodentate (nitrate and/or water) ligands. Owing to differences in the equatorial ligand field strengths, mono- and bischelation can be readily distinguished from each other by vibrational spectroscopy. Raman and infrared active vibration modes of uranyl undergo marked bathochromic shifts by increasing the number of bound hydroxamate anions. The main objective of this paper is to show to which extent the complexation of uranyl and iron with the model *N*-methylacetohydroxamate is similar. In order to gain a deeper insight into the interactions between the metals and NMA^- in the gas phase, we report the results of theoretical calculations (DFT) combined with experimental infrared multiphoton dissociation spectroscopic data (IRMPD) and other experiments.

RESULTS

Crystal Structure of $[\text{Fe}(\text{NMA})_3]\cdot\text{H}_2\text{O}$. The title complex was readily obtained by treating 3.4 equiv of NMAH with one equiv of $\text{Fe}(\text{acac})_3$ in methanol, followed by recrystallization of the isolated solid. Dark-red single crystals of $[\text{Fe}(\text{NMA})_3]\cdot\text{H}_2\text{O}$ having a plate-like shape were grown by diffusion of cyclohexane into a dichloromethane solution of the complex. Crystallographic parameters, data collection, and refinement information in tabular form are available in the Supporting Information. The complex crystallizes in the centrosymmetric space group $P2_1/n$ with two independent molecular units and two water solvent molecules (O7 and O8) per asymmetric unit (Figure 1). The independent units are interconnected to each other in an alternate fashion by each water molecule via hydrogen bonds involving the hydroxamic oxygen atoms, as O5 and O5A interact with both protons attached to O7, while O3 and O3A are bound to the O8 water molecule (Table S8 and Figure S1 in Supporting Information).

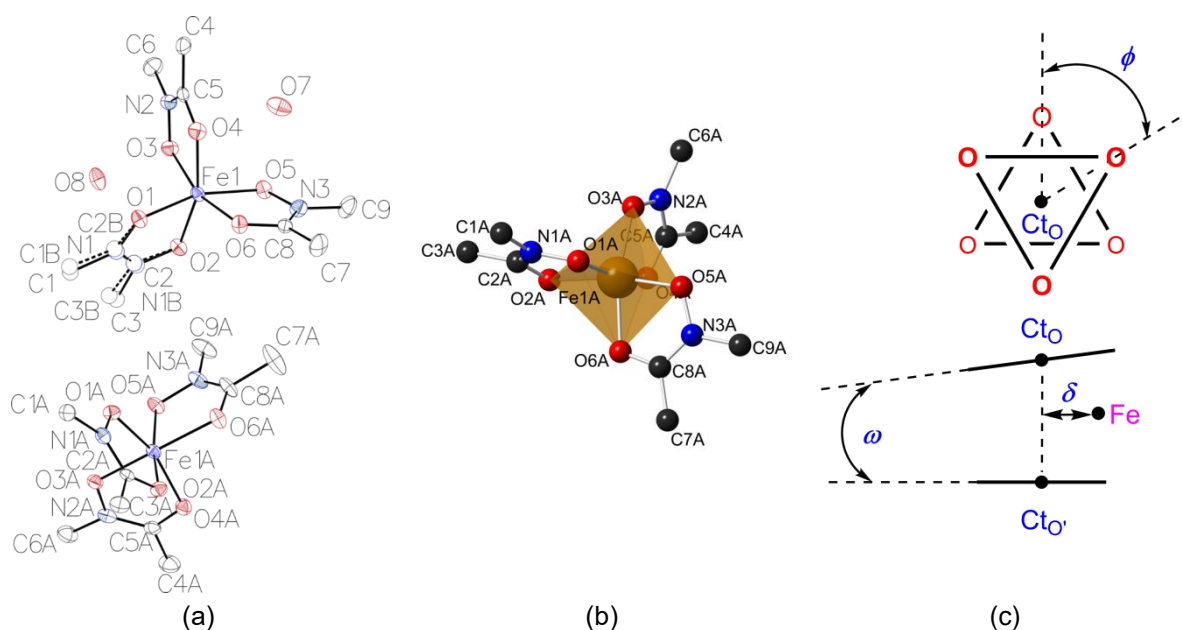


Figure 1. (a) ORTEP view of the asymmetric unit found in the crystal structure of $[\text{Fe}(\text{NMA})_3]\cdot\text{H}_2\text{O}$. Thermal ellipsoids are drawn at the 50% probability level and all protons are omitted for clarity. Disordered atoms were refined isotropically with site occupation

factors of 0.5. They are represented as non-shaded spheres connected by dashed bonds for one of the two-disordered fragment. (b) Ball-and-stick representation of the pseudo-octahedral coordination polyhedron of the crystallographically independent molecule labeled A. (c) Schematic representation of the pseudo-octahedral coordination polyhedron along the pseudo- C_3 axis (top) and from the side (bottom) defining the structural parameters ϕ , δ , and ω described in text. C_{T0} and $C_{T0'}$ are the centroids of each triplet of oxygen atoms defining both trigonal faces of the pseudo-octahedron.

Overall, bond distances for both $[\text{Fe}(\text{NMA})_3]$ molecules are quite similar. The arithmetic means determined for the most relevant bond types (2.01(2) Å for Fe–O, 1.295(5) Å for C=O, 1.360(5) Å for N–O, and 1.306(4) Å for C–N) are typical for iron(III) hydroxamic complexes (1.99(3) Å for Fe–O, 1.28(2) Å for C=O, 1.37(2) Å for N–O, and 1.32(3) Å for C–N) according to a statistical analysis encompassing the 190 entries retrieved from the CCDC database (Table S10 in Supporting Information). Relying on this clear C=O and N–O bond-length differentiation, electron densities in the Fourier maps could be easily assigned to the respective carbon and nitrogen atoms, although each of them is substituted with a methyl group. Likewise, O–Fe–O bite angles are similar for both structures, averaging 78.7(6)°, in perfect agreement with the literature data.

In both independent structures, the iron atom is bound to the six oxygen atoms provided by the three hydroxamate anions according to slightly-distorted octahedral coordination geometry, with quite regular Fe–O distances. Deviation from the ideal octahedral arrangement of the six donor atoms around the metal center (limiting O_h point group symmetry) can be described by several stereochemical parameters, such as the axial and equatorial O–Fe–O angles (180 and 90°, respectively for ideal O_h symmetry), the twist angle ϕ formed by both trigonal faces rotated along the C_3 axis ($\phi = 60^\circ$ in O_h), the tilt angle ω between both trigonal faces ($\omega = 0^\circ$ in O_h symmetry), the position ($C_{T0} \cdots \text{Fe} = C_{T0'} \cdots \text{Fe}$ in O_h , where C_{T0} designates the centroid of the triplet of oxygen atoms belonging to each trigonal face) and lateral displacement (δ) of the metal atom along the $C_{T0} \cdots C_{T0'}$ or C_3 axis ($\delta = 0$ Å in

O_h). A detailed analysis reveals a slightly more regular environment around Fe1 ($O_{ax}\text{--Fe--}O_{ax} = 162.5(8)^\circ$, $O_{ax}\text{--Fe--}O_{eq} = 90.15(8)\text{--}105.91(8)^\circ$, $\phi = -39(2)^\circ$, $\omega = 2.70^\circ$, $Ct_O \cdots Ct_{O'} = 2.292 \text{ \AA}$, $Ct_O \cdots Fe1 = 1.149 \text{ \AA}$, $Ct_{O'} \cdots Fe1 = 1.144 \text{ \AA}$, $\delta = 0.020 \text{ \AA}$) than around Fe1A ($O_{ax}\text{--Fe--}O_{ax} = 166(3)^\circ$, $O_{ax}\text{--Fe--}O_{eq} = 89.57(8)\text{--}100.45(8)^\circ$, $\phi = 44(2)^\circ$, $\omega = 3.34^\circ$, $Ct_O \cdots Ct_{O'} = 2.236 \text{ \AA}$, $Ct_O \cdots Fe1A = 1.103 \text{ \AA}$, $Ct_{O'} \cdots Fe1A = 1.133 \text{ \AA}$, $\delta = 0.031 \text{ \AA}$), while both coordination polyhedra have an opposite chirality.

An important parameter to consider for pseudo-octahedral ML_3 complexes is the normalized bite b ($b = O \cdots O/M\text{--}O$), averaging 1.272(6) and 1.267(9) for the three ligands chelated by Fe1A and Fe1, respectively. According to Kepert's electrostatic repulsion model, the stereochemistry is completely defined by only two parameters, namely the normalized bite and the twist angle ϕ between the upper and lower triangular faces, a perfect octahedron being achieved for $b = 2^{1/2}$.¹⁵ For smaller b values, the twist angle tends to decrease in order to minimize the repulsion energy. Assuming a symmetric bidentate chelate, the model predicts a ϕ value of 45.7° for $b = 1.27$, which conforms reasonably well to the observed angles.

Owing to the nonsymmetrical structure of the NMA^- ligand, the trichelated $[Fe(NMA)_3]$ complex is supposed to form a statistical 1:3 mixture of *fac* and *mer* isomers in solution. Interestingly, this ratio is reversed in the crystal state. Indeed, the crystallographically independent molecule labeled A contained in the asymmetric unit possesses a *fac* arrangement, while the carbon and nitrogen atoms of one NMA^- ligand bound to Fe1 are split over two positions (N1/C2B, C1/C1B, C2/N1B, C3/C3B) with equal site occupation factors (Figure 1 and Table S9 in Supporting Information). Hence, half of the Fe1 molecular units correspond also to the *fac* isomer for which all chelates adopt the same directionality, while for the other half one chelate among the three is coordinated in the reversed sense, giving rise to the *mer* isomer.

Gas Phase Structures of Iron Complexes. Electrospray ionization of a methanolic solution of a genuine sample of $[\text{Fe}(\text{NMA})_3] \cdot 0.6\text{H}_2\text{O}$ produces $[\text{Fe}_n(\text{NMA})_{3n-1}]^+$ ($n = 1$ and 2) cluster ions (Figure S4 in Supporting Information). We have investigated the dinuclear cluster $[\text{Fe}_2(\text{NMA})_5]^+$ ($m/z = 552$). The collision-induced dissociation of this cation leads to the elimination of one or two *N*-methylacetohydroxamate radicals (Figure S5 in Supporting Information). The structure of the $[\text{Fe}_2(\text{NMA})_5]^+$ cation was further probed by infrared multiphoton dissociation spectroscopy (IRMPD). IRMPD spectroscopy provides IR spectra of mass-selected ions.¹⁶ The absorption of photons induces fragmentation of the mass-selected ions that is detected by mass spectrometry. Dependence of the fragmentation yield on the photon energy provides the IRMPD spectrum. The IRMPD spectra are multiphotonic (typically many photons have to be absorbed in order to induce the fragmentation of the given ion) and the peak intensities therefore do not linearly correlate with the intensities expected in the single-photon spectra (classical IR spectra, theoretical IR spectra). It can be difficult or impossible to obtain IRMPD spectra for ions with high-energy fragmentation thresholds. This is the case for the $[\text{Fe}(\text{NMA})_2]^+$ monomer, therefore only the dimer has been investigated here.

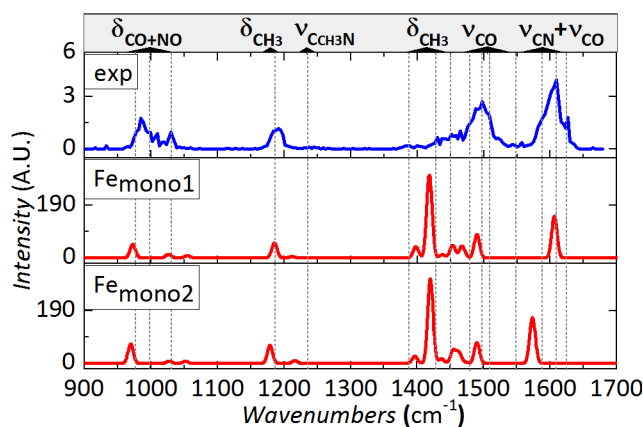


Figure 2. Comparison of the IRMPD spectrum of $[\text{Fe}_2(\text{NMA})_5]^+$ (m/z 552; fragments with m/z 464 and 376 were monitored during IRMPD) and the theoretical IR spectra calculated for ${}^4\text{Fe}_{\text{mono}1}$ and ${}^6\text{Fe}_{\text{mono}2}$. The harmonic frequencies were scaled by a factor of 0.99. The panel on the top shows the peak attribution derived from the normal-mode analysis (see Table S13 in Supporting Information for the full assignment).

The IRMPD spectrum of $[\text{Fe}_2(\text{NMA})_5]^+$ contains four dominant composite bands at 976, 1183, 1496, and 1605 cm^{-1} (Figure 2). We have assigned the bands based on comparison with theoretical IR spectra (B3LYP/SDD/cc-pVTZ) of relevant complexes. In the first approximation, we modelled a simple mononuclear complex $[\text{Fe}(\text{NMA})_2]^+$. Two coordination modes are possible around Fe^{3+} , either a square-planar ($\text{Fe}_{\text{mono}1}$) or a tetrahedral ($\text{Fe}_{\text{mono}2}$) arrangement. The B3LYP method predicts the quartet ($S = 3/2$) and the sextet ($S = 5/2$) ground state for ${}^4\text{Fe}_{\text{mono}1}$ and ${}^6\text{Fe}_{\text{mono}2}$, respectively (Figure 3). In comparison with neutral *N*-methylacetohydroxamic acid and its anion (Table S17 in Supporting Information), the geometries of the acetohydroxamate ligands suggest much larger delocalization of the non-bonding electrons from the nitrogen atom towards the carbonyl carbon atom (i.e. larger contribution of the third resonance structure in Figure 3c). This leads to a contraction of the central C–N bond and an elongation of the carbonyl C=O bond (see the green values in Figure 3). The changes are slightly more pronounced for the ${}^4\text{Fe}_{\text{mono}1}$.

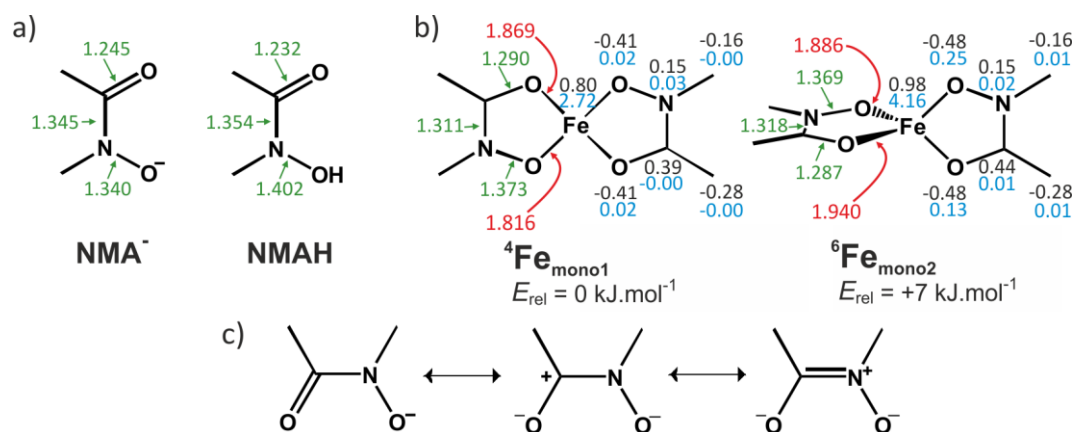


Figure 3. B3LYP optimized structures of (a) *N*-methylacetohydroxamate and *N*-methylacetohydroxamic acid, and (b) the square-planar (⁴Fe_{mono1}) and tetrahedral (⁶Fe_{mono2}) isomers of the [Fe(NMA)₂]⁺ complex together with their relative energies. Numbers in green are bond distances (in red for Fe–O distances) in Angströms (Å), those in black are the Mulliken charges and the ones in blue are the Mulliken spin distributions. (c) Resonance structures of (Z)-NMA⁻.

The calculated IR spectra corresponding to ⁴Fe_{mono1} and ⁶Fe_{mono2} are almost identical with the exception of the $\nu(\text{C-N})$ stretching mode (Figure 2 and Table S13 in Supporting Information). It is found at 1603 cm⁻¹ for the square-planar isomer ⁴Fe_{mono1} and at 1572 cm⁻¹ for the tetrahedral isomer ⁶Fe_{mono2}. The higher frequency of the C–N stretching mode in ⁴Fe_{mono1} compared to ⁶Fe_{mono2} is in accord with larger geometry changes in this isomer resulting in the shorter C–N bond.

The bands at 1496 and 1605 cm⁻¹ in the IRMPD spectrum can be thus assigned to the carbonyl stretching and the C–N stretching, respectively. Compared to the spectrum of NMA⁻ (Figures S8–S9 and Table S12 in Supporting Information), the coordinated ligands reveal a considerable red-shift of the C=O vibration ($\Delta\nu = 138 \text{ cm}^{-1}$) and a blue shift of the C–N vibration. This is associated with the electron delocalization and geometry changes described above. The tentative assignment of the other bands is shown in Figure 2, the detailed discussion can be found in the in the Supporting Information.

The comparison with the results expected for the mononuclear complex helps in the assignment of the dominant bands, but cannot account for the whole IRMPD spectrum of

$[\text{Fe}_2(\text{NMA})_5]^+$. Therefore, we refined the study by computing the structures and IR spectra of binuclear complexes $[\text{Fe}_2(\text{NMA})_5]^+$. The most stable structures possess always an octahedral coordination sphere around both iron centers and we assumed only high-spin complexes (other spin state combinations led to severe problems with the convergence of the calculations). However, the bridging mode between the two iron(III) atoms can differ. Here, we present four structures with different bridging modes (**Fe_{di1}**, **Fe_{di2}**, **Fe_{di3}**, **Fe_{di4}** in Figure 4a). In **Fe_{di1}** and **Fe_{di2}**, two hydroxamate ligands are bridging the iron centers via a single oxygen ($\mu_{1,1}$ binding) having different ligand orientations. In **Fe_{di4}**, one additional NMA[−] ligand connects both irons through two oxygen atoms in a $\mu_{1,4}$ mode. **Fe_{di3}** was calculated with **Fe_{di1}** as the starting structure, but the $\mu_{1,1}$ -bridging oxygen (in the back) is linked to the carbon instead of the nitrogen atom.

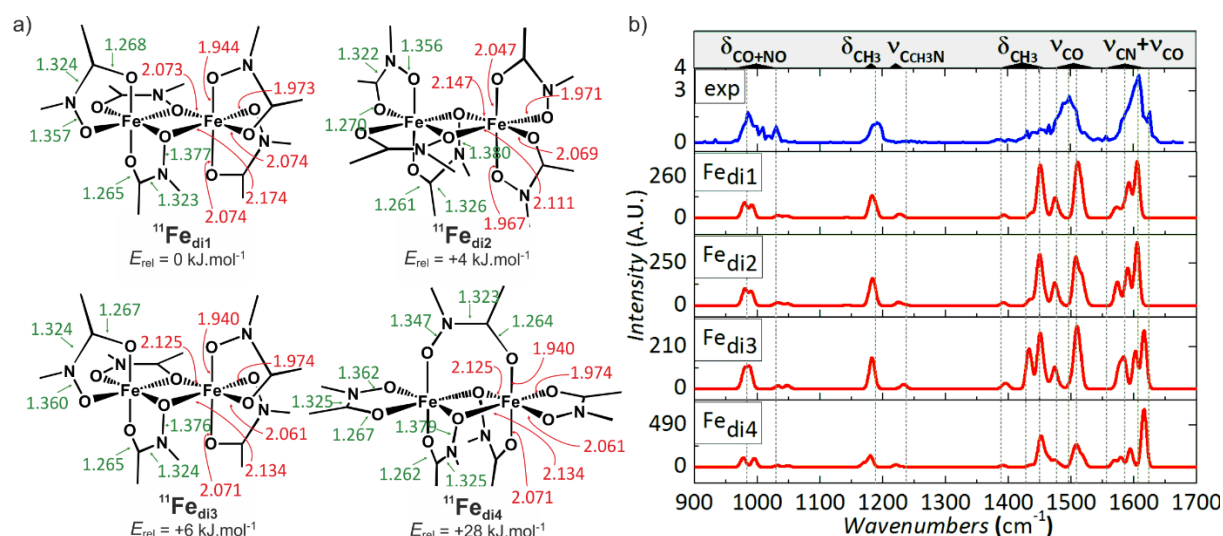


Figure 4. (a) Structure of the four possible isomers of $[\text{Fe}_2(\text{NMA})_5]^+$ (**Fe_{di1}**, **Fe_{di2}**, **Fe_{di3}**, and **Fe_{di4}**, optimized geometries can be found in the SI). Numbers in green correspond to selected bonding distances in Angströms (Å), while those in red refer to the Fe–O distances. (b) IRMPD spectrum of the $[\text{Fe}_2(\text{NMA})_5]^+$ ion (identical to Figure 2) and theoretical spectra of **Fe_{di1}**, **Fe_{di2}**, **Fe_{di3}**, and **Fe_{di4}**. The harmonic frequencies were scaled by a factor of 0.99. The panel on the top shows the peak assignment derived from the normal-mode analysis (see Table S14 in Supporting Information for the full assignment).

The relative energies found for complexes **Fe_{di1}**, **Fe_{di2}**, **Fe_{di3}**, and **Fe_{di4}** are 0, +4, +6,

+28 kJ mol⁻¹, respectively. Energetically, the complexes having only two $\mu_{1,1}$ -oxygen bridges between both iron atoms (**Fe_{di1-3}**) are more stable than the complex containing one additional ligand bridging the two metal centers (**Fe_{di4}**) in a $\mu_{1,4}$ fashion. The comparison of **Fe_{di1}** and **Fe_{di2}**, shows that the bridging-ligand orientation affects the overall stability of the complex only little (4 kJ mol⁻¹). Bridging by the oxygen atom linked to the nitrogen atom as in **Fe_{di1}** provides a more stable assembly than the bridging by the carbonyl oxygen atom as in **Fe_{di3}** ($\Delta E = 6$ kJ mol⁻¹).

The calculated IR spectra for all four isomers are rather similar, as all evidence four composite bands that are also present in the experimental IRMPD spectrum (Figure 4b). Considering the experimental spectral resolution (ca. 20 cm⁻¹) and the rather high resemblance of the theoretical spectra, the gas-phase structure of the [Fe₂(NMA)₅]⁺ cation cannot be unambiguously assigned. Keeping in mind that the calculated energy difference between the most stable **Fe_{di1}** and **Fe_{di2}** isomers ($\Delta E = 4$ kJ mol⁻¹) is below the accuracy of the theoretical calculations, the occurrence of both species in equilibrium is highly probable. Furthermore, the experimental trace in Figure 4b evidences an additional band at higher wavenumbers (1620 cm⁻¹), suggesting that some species possess a bridging carbonyl oxygen atom such as found in structure **Fe_{di3}**, which lies only 6 kJ mol⁻¹ in energy above **Fe_{di1}**. Therefore, the feature at 1620 cm⁻¹ can originate from a contribution of **Fe_{di3}**. The highly-strained $\mu_{1,4}$ -bridged **Fe_{di4}** structure also evidences a carbonyl stretch around 1620 cm⁻¹, but its experimental detection is unlikely because of its high energy ($\Delta E = +22$ and + 28 kJ mol⁻¹ with respect to **Fe_{di1}** and **Fe_{di3}**, respectively). The experimental spectrum can thus be best described as a superposition of individual components arising from several isomers (i.e. **Fe_{di1-3}**).

The composite experimental band at 1605 cm⁻¹ is nicely reproduced by theory, suggesting different binding modes of the hydroxamate ligand (either analogous to the one

found in the square-planar monomer **Fe_{mono1}**, the tetrahedral monomer **Fe_{mono2}**, or as bridging both iron-centers). Similarly to the theoretical spectra of monomers, the intensity of the CH₃ deformation modes centered at 1450 cm⁻¹ is much larger than the experimentally recorded one. This enhancement can be either a consequence of the mixing with the C=O stretching, but the experimental intensities can also be underestimated due to the multiphoton nature of the IRMPD method.

Gas Phase Structures of Uranyl Complexes. A mass spectrum of a methanolic solution of [UO₂(NMA)₂(H₂O)] shows formation of a variety of [UO₂²⁺(NMA)(L)_{*n*}] complexes with L = NMAH, H₂O, or CH₃OH and *n* = 0–2 (Figure S8 in Supporting Information). Assignments given in Table S11 were confirmed by (+)-HR-ESI-MS spectroscopy (Figure S9 in Supporting Information) together with simulations of the isotopic patterns. We have further investigated only complex [UO₂(NMA)(NMAH)₂]⁺ bearing one hydroxamate and two neutral hydroxamic acids as ligands.

The IRMPD spectrum of the mass-selected [UO₂(NMA)(NMAH)₂]⁺ cation (*m/z* = 536; Figure 5b) looks at first sight very similar to the spectrum of the iron complex discussed above. It suggests a similar effect of the UO₂²⁺ core on hydroxamate ligands as was found for Fe³⁺. The spectrum can be divided into four different regions: 900–1000, 1150–1250, 1400–1500, and 1550–1650 cm⁻¹. Each range contains several overlapping bands reflecting binding modes of each ligand. The detailed assignment can be found in Table S15 in Supporting Information.

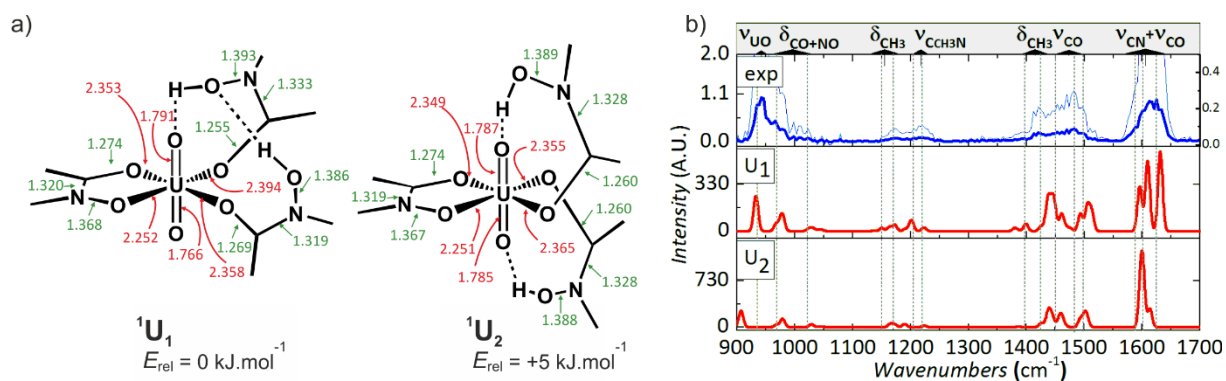


Figure 5. (a) Structure of possible isomers U_1 and U_2 of $[\text{UO}_2(\text{NMA})(\text{NMAH})_2]^+$ (optimized geometries can be found in the SI). Numbers in green refer to selected bonding distances in Angströms (\AA), while those in red refer to the U–O distances. (b) IRMPD spectrum of the $[\text{UO}_2(\text{NMA})(\text{NMAH})_2]^+$ cation ($m/z = 536$; fragments with m/z 518 and 447 and its water adduct with m/z 465 were monitored during IRMPD) and theoretical spectra of U_1 and U_2 . A scaling factor of 0.985 was applied to all harmonic frequencies. The panel on the top shows the peak assignments derived from the normal-mode analysis. The thin blue line is a zoom of the experimental spectrum magnified 4 times, the corresponding scale appearing on the right side (see Table S15 in Supporting Information for the full assignment).

The linear UO_2^{2+} cation (the "yl" oxygen atoms define the axial positions) typically interacts with four to six oxygen-bound ligands in the equatorial plane.¹⁷ All our attempts in optimizing the structure of the triply ligated complex $[\text{UO}_2(\text{NMA})(\text{NMAH})_2]^+$ resulted in octahedral coordination with just four U–O bonds in the equatorial plane. All attempts to put five or more U–O bonds in the equatorial plane failed and the calculations invariably converged to stable structures with only four equatorial oxygen atoms. Two of these donor atoms are provided by the bidentate *N*-methylacetohydroxamate (NMA^-) ligand. The two remaining oxygens are the carbonyl oxygen atoms of both neutral *N*-methylacetohydroxamic acids (NMAH). The N–OH groups of the monodentate NMAH molecules are available for intramolecular hydrogen bonds. In the most stable structure U_1 (Figure 5a), the OH group of one *N*-methylacetohydroxamic acid makes a H-bond with one "yl" oxygen atom of the UO_2^{2+} core, while the second hydroxyl group interacts with the neighboring N–OH oxygen atom. In the second most favored structure (U_2), both monodentate NMAH molecules are hydrogen-

bonded to the opposite uranyl oxygen atoms.

The various bending modes of the CH₃ substituents are spread over the 900–1500 cm⁻¹ region and are, as expected, not very sensitive to the structural differences between **U**₁ and **U**₂. The situation is markedly different in the 1500–1700 cm⁻¹ range, since **U**₁ gives rise to three different C–N stretching frequencies (1623, 1604, and 1587 cm⁻¹), owing to the differences in the binding mode and protonation state of the three ligands. Both bands at 1604 and 1623 cm⁻¹ correspond to the two protonated NMAH ligands, while the lower-energy band at 1587 cm⁻¹ is assigned to the stretching mode for the deprotonated anionic hydroxamate ligand. The same order is observed for the C=O stretching bands: those at 1498 and 1505 cm⁻¹ are associated to the NMAH molecules and that centered at 1486 cm⁻¹ to the bidentate NMA⁻ anion. Experimentally, only poorly resolved overlapping bands are observed instead of the three distinct peaks.

The IRMPD spectrum of [UO₂(NMA)(NMAH)₂]⁺ corresponds rather well to the IR spectrum calculated for **U**₁ (Figure 5b). Especially in the ranges around 950 and 1600 cm⁻¹ the spectrum is well reproduced by the theoretical IR spectrum of **U**₁, whereas the prediction for **U**₂ is not matching. The O=U=O antisymmetric stretching mode (ν_{as}) of the uranyl cation is observed at 944 cm⁻¹ by IRMPD (a comparison with literature data can be found in the Supporting Information). Remarkably, the wavenumber computed for **U**₁ (933 cm⁻¹, see Table S15 in Supporting Information) agrees fairly well with the experimental value, which is consistent with a hydrogen bond being formed to only one of the oxygen atoms. In turn, hydrogen bonding to both uranyl oxygen atoms as found in **U**₂ gives rise to an absorption band located near 900 cm⁻¹ (Figure 5b), inconsistent with the experimental findings.

Water Elimination from [UO₂(NMA)(NMAH)₂]⁺. The collision induced dissociation (CID) experiment with [UO₂(NMA)(NMAH)₂]⁺ ($m/z = 536.172$) shows that the

complex easily loses a molecule of water ($m/z = 518.162$) or one NMAH ligand ($m/z = 447.125$) (Figure S10 in Supporting Information). The elimination of NMAH can be followed by secondary reactions with background gases, H₂O and CH₃OH, yielding [UO₂(NMA)(NMAH)(H₂O)]⁺ and [UO₂(NMA)(NMAH)(CH₃OH)]⁺.

The eliminated water molecule can contain either the oxygen atom from a coordinated ligand or from one U=O bond of the uranyl cation. The activation of the U=O bond and thus elimination of the uranyl oxygen atom was proved by CID of isotopically labelled [U¹⁸O₂(NMA)(NMAH)₂]⁺. The CID clearly shows exclusive elimination of H₂¹⁸O (Figure S11 in Supporting Information). Further, the structure of the dehydrated complex ($m/z = 518$) was investigated by IRMPD spectroscopy (blue curves in Figure 6). Contrary to the parent ion, the IRMPD spectrum of the dehydrated complex does not contain the intense band at about 940 cm⁻¹ corresponding to the O=U=O antisymmetric stretching. The bands corresponding to the C–N and C=O stretchings are broad, overlapping, and slightly redshifted. The disappearance of the uranyl vibration mode suggests formation of a UO⁴⁺ complexed species.

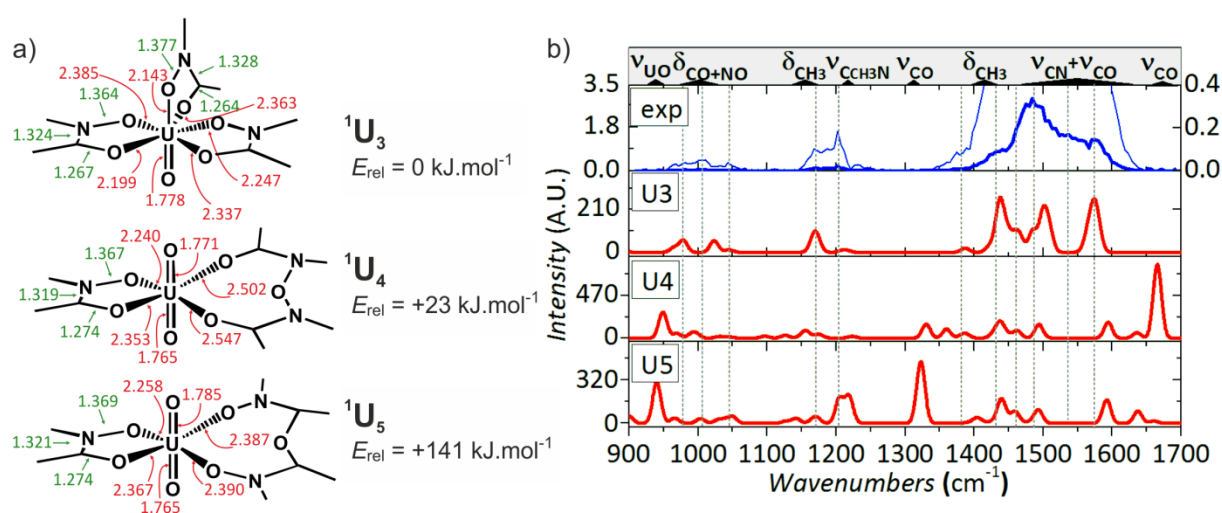


Figure 6. (a) Structure of the possible isomers U₃, U₄, and U₅ formed by water elimination from [UO₂(NMA)(NMAH)₂]⁺ (optimized geometries can be found in the SI). Numbers in green refer to selected bond distances in Angströms (Å), while those in red refer to the U–O

distances. (b) IRMPD spectrum of the dehydration product ($m/z = 518$, fragments with m/z 430 and its water adduct with m/z 448 was monitored) generated by CID of the parent ion $[\text{UO}_2(\text{NMA})(\text{NMAH})_2]^+$ ($m/z = 536$) and theoretical spectra of **U**₃, **U**₄, and **U**₅. A scaling factor of 0.99 was applied to all harmonic frequencies. The panel on the top shows the peak attribution derived from the normal-mode analysis. The thin blue line is a zoom of the experimental spectrum magnified 8.75 times, the corresponding scale appearing on the right side.

Possible structures of the dehydrated complex were optimized by DFT computations. The three arrangements of lowest energy are shown in Figure 6a. These calculations suggest that the most stable species (**U**₃) contains indeed a monooxo uranium cation. Moreover, the theoretical IR spectrum of **U**₃ is perfectly consistent with the experimental IRMPD spectrum (Figure 6). The other possibilities demonstrate that elimination of water from two in-plane hydroxamic ligands (**U**₄ and **U**₅) is disfavored by energetics and the products have IR spectra inconsistent with the experimental results.

We have further probed, whether fragmentations of uranyl complexes incorporating on one or two NMA^-/NMAH ligands would also lead to the $\text{U}=\text{O}$ bond activation. The CID spectrum of the isotopically labeled $[\text{U}^{18}\text{O}_2(\text{NMA})(\text{NMAH})]^+$ ion ($m/z = 451.136$) shows elimination of $\text{CH}_3\text{N}^{16}\text{O}$ ($M_r = 45.021$) and NMAH ($M_r = 89.047$), but no sign of $\text{U}=\text{O}^{18}$ activation (Figure S12 in Supporting Information). Similarly, CID of $[\text{U}^{18}\text{O}_2(\text{NMA})(\text{CH}_3\text{OH})]^+$ ($m/z = 394.114$) does not reveal any process involving the $\text{U}=\text{O}^{18}$ bond (Figure S13 in Supporting Information). Accordingly, the loss of the uranyl oxygen atom for the $\text{UO}_2^{2+}/\text{NMA}^-$ system is associated with the structure of $[\text{UO}_2(\text{NMA})(\text{NMAH})_2]^+$. The postulated apical $\text{U}=\text{O}\cdots\text{HO}-\text{N}$ hydrogen bond in **U**₁ provides an opportunity for a facile hydrogen transfer from the ligand to the uranyl oxygen atom. The formation of the hydroxyl group will be associated with bidentate coordination of the formed anionic ligand. This process will lower the energy barrier for the second proton transfer, which ultimately leads to the elimination of water.

DISCUSSION

Similarities and Differences of Iron and Uranyl Complexes. Good agreement between experimental IRMPD and theoretical IR spectra enables us to discuss in more details relevant structural properties. The following analysis encompasses the selected ligand NMA^- and its protonated form NMAH, as well as the $\mathbf{Fe}_{\text{mono1}}$, \mathbf{Fe}_{di1} , and \mathbf{U}_1 complexes. Relevant bond distances retrieved from each DFT-optimized structure are reported in Table S17 (Supporting Information) and shown in Figures 3–5. Calculated C=O (1.23 Å) and C–N (1.35 Å) bonds distances for NMAH are in perfect agreement with the data reported in the literature for hydroxamic acids (1.23 and 1.34–1.40 Å, respectively).¹⁸ Structural parameters obtained in this work for the diferric $[\text{Fe}_2(\text{NMA})_5]^+$ (\mathbf{Fe}_{di1}) complex (1.94–2.06 Å for Fe–O, 1.27 Å for C=O, 1.36–1.38 Å for N–O, and 1.32 Å for C–N) are also reproducing well the crystallographic distances determined herein for the neutral $[\text{Fe}(\text{NMA})_3]$ complex (2.01(2) Å for Fe–O, 1.295(5) Å for C=O, 1.360(5) Å for N–O, and 1.306(4) Å for C–N) and those reported by Dhungana et al. for the ferrioxamine B complex (1.981 Å for Fe–O_N, 2.037 Å for Fe–O_C, 1.282 Å for C=O, 1.377 Å for N–O, 1.317 Å for C–N).¹⁹

In the case of the $[\text{UO}_2(\text{NMA})(\text{NMAH})_2]^+$ (\mathbf{U}_1) cationic species, average axial U=O (1.78 Å) and equatorial U–O (2.37 Å) bond lengths are similar to those found by X-ray diffractometry for $[\text{UO}_2(\text{NMA})(\text{NO}_3)(\text{H}_2\text{O})_2]$ (U=O = 1.770(1) Å, U–O_N = 2.387(3) Å, U–O_C = 2.396(3) Å).³ Overall, binding of NMA^- to iron or uranium produces similar changes: C=O, N–O, and N–C_{Me} bonds are getting longer, while C–N and C–C_{Me} bonds are shortened when compared to the free hydroxamate ligand (Figures 3–5). These expected trends are also consistent with the shifts undergone by the corresponding vibration frequencies. The only noticeable difference between the iron and uranium complexes is the longer metal-oxygen

distance for the latter species as stressed above (2.37 vs. 1.94–2.06 Å), which is consistent with the larger radius of the uranium atom ($r_i = 0.73$ vs. 0.645 Å for hexacoordinated uranium(VI) and high-spin iron(III), respectively).²⁰

Comparison of the Bond Nature in the Iron and Uranyl Complexes. Both optimized structures of the **Fe_{mono2}** and **U₁** complexes were subjected to the Natural Bond Orbitals (NBO) analysis to gauge the covalent character of the metal-ligand interactions occurring in the gas phase (Table S18 in Supporting Information). The electronic natural configurations determined by the NBO analysis are [core]4s^{0.25}3d^{5.85}4p^{0.37}4d^{0.01} with a charge of 1.51 at the iron(III) in complex **Fe_{mono2}** and [core]7s^{0.15}5f^{2.60}6d^{1.36}7p^{0.32} with a charge of 1.72 at the uranium in the uranyl complex **U₁**. The number of d-electrons on Fe(III), close to 6, can be explained by a ligand-to-metal charge transfer, which is a well-known characteristic of iron-hydroxamate complexes responsible for their orange-red color.²¹ The electronic configuration of uranium is similar to the one reported before for an uranium(VI) phosphopeptide complex (2.60 and 1.40 respectively for 5f and 6d orbitals).²²

The similarity of the NBO charges in both complexes suggests that the bonding of the ligands should be of similar nature. Barros et al. proposed that the ratio between the NBO charge and the oxidation number of the metal should be a good descriptor of a covalent or ionic nature of the metal-ligand interactions in a complexed species.²³ The lower this ratio, the more covalent are the bonds, due to a greater sharing of electrons. The calculated ratios for **Fe_{mono2}** and **U₁** are 0.50 and 0.29, respectively, suggesting that bonds to uranium(VI) are more covalent than those to iron(III). It is important to note that the Barros ratio reflects the sum of all ionic and covalent contributions of all ligands around the metal. In the case of **U₁**, NBO analysis reveals that both U=O_{y1} bonds are the main contribution to the overall high covalence, whereas the equatorial oxygen atoms show partially ionic interactions (Table S18

in Supporting Information). Hence, while the polarization of the U=O_{yl} bonds is 79% for O and 21% for U, we found an average value of about 89% for O and 11% for U for the equatorial bonds to the hydroxamates. The NBO analysis reveals multiple character of the U=O_{yl} bond, whereas there is just a single bond between U and the oxygen atoms of the hydroxamates.

In the case of **Fe_{mono2}**, the NBO analysis reveals a similar character of all Fe–O bonds with an average electron density polarization of the Fe–O bonds of 85% at oxygen and 15% at iron (Table S18 in Supporting Information). This finding agrees with the study of Domagal-Goldman et al.,²⁴ who assigned the high stability of the iron(III) complex with desferrioxamine B ($\beta_{\text{Fe}(\text{DFB})\text{H}} = 10^{30.6}$) at least to some extent to the covalent contribution. Interestingly, their NBO analysis showed no indication of covalence for the analogous iron(II) or aluminum(III) complexes.

From these findings, it can be concluded that Fe^{III}–O and U^{VI}–O_{eq} bonds constituted by hydroxamate anions and hydroxamic acids are highly-polarized covalent bonds, as typically expected for hard acid-hard base complexes.²⁵ The M–O bonds in the uranium complex [UO₂(NMA)(NMAH)₂]⁺ (**U₁**) are slightly more polarized than those occurring in [Fe(NMA)₂]⁺ (**Fe_{mono2}**). It most likely originates from the differences in orbital shapes and overlapping with the ligand orbitals (uranium 4f-orbitals overlap less well with the s and p orbitals of the ligand than the 3d orbitals of iron do).

U=O Bond Activation. Fragmentation experiments on several monovalent cations produced by electrospray ionization of methanolic solutions of the [UO₂(NMA)₂(H₂O)] complex revealed an unexpected behavior specific to the [UO₂(NMA)(NMAH)₂]⁺ gas-phase species, which translates into abstraction of an "yl" oxygen atom from the uranyl core and the concomitant elimination of a water molecule. Reputed as particularly inert, both U=O bonds in UO₂²⁺ are extremely difficult to activate and typically undergo reduction upon silylation or

reaction with strong Lewis acids. Direct bond cleavage initiated by ESI-MS CID of coordinated uranyl cations has only been achieved very recently for a few number of systems, although none incorporated a chelating ligand nor eliminated a molecule of water.²⁶ CID of $[\text{UO}_2(\text{N}_3)\text{Cl}_2]^-$ produces the nitrosyl complex $[\text{UO}(\text{NO})\text{Cl}_2]^-$ together with N_2 , $[\text{UO}_2(\text{NCO})\text{Cl}_2]^-$ decomposes into $[\text{UONCl}_2]^-$ and CO_2 , while $[\text{UO}_2(\text{CH}_3\text{CN})]^{2+}$ generates the intermediate cation $[\text{UO}_2(\text{NC})]^+$ that fragments into UON^+ and CO . Most remarkably, the ever-first example of double activation for an uranyl complex in the gas phase has been reported in fall 2017 by Abergel et al.²⁷ MS-MS analysis of the tetracatecholamide $[\text{UO}_2(3,4,3\text{-LI-CAM})\text{H}_5]^-$ anion produced a heptacoordinated U^{6+} chelate of $[\text{U}(3,4,3\text{-LI-CAM})\text{H}]^-$ formula upon simultaneous release of two water molecules, as ascertained by IRMPD and ^{18}O -labeling experiments.

In that context, our present findings provide an additional example for U=O bound activation, most likely promoted by hydrogen bond interactions involving the abstracted "yl" oxygen atom in the parent ion. In the case of $[\text{UO}_2(3,4,3\text{-LI-CAM})\text{H}_5]^-$, the OH groups from the catechol units bound to uranyl in the equatorial plane, as well as those remaining unbound but located in close vicinity to the coordination center, play a prominent role in the activation process. Transfer of exchangeable protons from neighboring donor groups is an essential step in the formation of water, as this process is expected to lower the energy barrier of the U=O bond rupture. Here, $[\text{UO}_2(\text{NMA})(\text{NMAH})_2]^+$ provides the ever first case of bond activation through water elimination that is favored by a direct hydrogen bond between the apical O_{yl} atom and one hydroxyl group from a coordinated ligand.

These findings have also some relevance to the chemical properties of uranyl in the condensed phase. While its oxygen atoms are reputed inert in the ground state, albeit exchange occurs rapidly in the excited state upon UV irradiation, dramatic enhancement of the lability of the O_{yl} atoms in aqueous solutions has been observed by Szabó and Grenthe for

the $[(\text{UO}_2)_2(\mu\text{-OH})_2(\text{H}_2\text{O})_6]^{2+}$ species.²⁸ These authors evidenced a fast exchange with the oxygen atoms provided by bulk water for that particular hydrolyzed species, with a half-life of 0.13 s and an activation enthalpy of 80(14) kJ/mol for the rate determining step. Conversely, no appreciable oxygen exchange could be detected by ^{17}O NMR spectroscopy for UO_2^{2+} , $\text{UO}_2(\text{OH})^+$, $\text{UO}_2(\text{OH})_4^{2-}$, $\text{UO}_2(\text{OH})_5^{3-}$, and for the ternary complex $[(\text{UO}_2)_2(\mu\text{-OH})_2\text{F}_2(\text{oxalate})_2]^{4-}$, suggesting that exchange only takes place in polynuclear hydroxide complexes, provided water molecules are present in the first coordination shell. The suggested mechanism involves a proton transfer from water molecules bound in the equatorial plane to the “yl”-oxygen that weakens the U=O interaction, followed by a rapid exchange of the resulting OH group with the bulk water. As a matter of fact, the U=O bond reactivity in the gas-phase and in solution shares some common features, namely the pivotal role of the hydroxyl group and the presence of an additional proton donor.

CONCLUSION

Complexation of Fe^{3+} and UO_2^{2+} with *N*-methylacetohydroxamate are qualitatively of the same nature, as evidenced by the bond distances and the IR spectra. The M–O bonds between the metal (M = U or Fe) and the oxygen atom of hydroxamate can be described as highly polarized covalent bonds. The interaction of the hydroxamate ligands with the uranyl results in slightly more polarized M–O bonds than the interaction with iron(III). The hydroxamate moiety is affected in the same way upon binding to either iron or uranyl: the carbonyl bond elongates, owing to the extended conjugation, while the C–N bond shortens as it gains a double-bond character. The geometry changes are evidenced by the red- and blue shifts of the corresponding IR absorption bands, respectively. The gas-phase uranium complex $[\text{UO}_2(\text{NMA})(\text{NMAH})_2]^+$ easily eliminates a water molecule upon collisional activation.

IRMPD spectroscopy, DFT computations, and MS-MS measurements performed with natural and ^{18}O -enriched uranyl samples suggest that the fragmentation involves the uranyl oxo ligand. The fragment ions thus have only one oxo ligand and three bidentally coordinated hydroxamates. In the context of depollution and complexation of uranium, these results show that a siderophore can bind also strongly to uranium(VI), but specific reactivity can arise in the gas phase from the oxygen of the “yl” moiety.

EXPERIMENTAL SECTION

CAUTION! Uranium (primary isotope ^{238}U) is a weak α -emitter (4.197 MeV) with a half-life of 4.47×10^9 years. All complexes were synthesized in monitored fume hoods, in a laboratory equipped with α - and β -counting equipment.

Materials and Methods. All solvents and analytical-grade chemicals were obtained from commercial suppliers and used without further purification. *N*-methylacetohydroxamic acid (NMAH) was prepared following the improved procedure described recently by Brandès et al.³ The sample used herein was taken from the same batch for which analytical data (^1H and ^{13}C NMR, CHN contents) have been reported elsewhere.³ An aqueous stock solution of ^{18}O -labeled uranyl (0.185 mol/kg) was prepared by dissolving 52.13 mg of $[\text{UO}_2(\text{NO}_3)_2(\text{H}_2\text{O})_2] \cdot 4\text{H}_2\text{O}$ with 561.39 mg of H_2^{18}O (Sigma-Aldrich, 97% ^{18}O) directly in a stoppered fluorescence quartz cell of 1 cm path length. The cuvette was exposed for ca. 180 h to UV radiations in the center of a Luzchem ring illuminator equipped with two 22 W mercury UVA lamps, after which the solution was acidified to $\text{p}[\text{H}] \sim 1.0$ by adding 3 μL of 69% HNO_3 (~ 15.4 M, Fischer, Trace Analysis). The enrichment level was monitored as a function of irradiation time by (+)-HR-ESI-MS after diluting 500 times the stock solution in

analytical-grade methanol. Integration of the isotopic pattern of the UO_2^+ signal gave 80% of $\text{U}^{18}\text{O}_2^+$ ($m/z = 274.04$), 17% of $\text{U}^{16}\text{O}^{18}\text{O}^+$ ($m/z = 272.04$), and 3% of residual $\text{U}^{16}\text{O}_2^+$ ($m/z = 270.04$). The almost complete oxygen exchange was confirmed by Raman spectroscopy with the total disappearance of the signal at 870 cm^{-1} ($\nu_s(\text{U}=\text{O})$) and the occurrence of a strong band at 824 cm^{-1} ($\nu_s(\text{U}=\text{O})$), assigned to the fully labeled $\text{U}(\text{O})_2^+$ cation. The weak foot-hump at $\sim 850\text{ cm}^{-1}$ agrees with the presence of a small amount of partially labeled $\text{U}^{16}\text{O}^{18}\text{O}^{2+}$ in the mother solution.

Fourier-transform mid-infrared ($400\text{--}4000\text{ cm}^{-1}$) spectra (FTMIR) were recorded at 4 cm^{-1} resolution on a Bruker VERTEX 70v spectrometer fitted with an A225 diamond attenuated total reflection (ATR) accessory (Bruker) and a DTGS (deuterated triglycine sulfate) detector ($350\text{--}4000\text{ cm}^{-1}$). Raman spectra were collected with a Renishaw inVia spectrometer equipped with a 632.8 nm He-Ne laser excitation source, a 1800 grooves/mm grating, and a microscope fitted with either a $\times 50$ (solid samples) or $\times 20$ (liquid samples) objective. Solids were deposited on a glass slide, while solutions were introduced in a fluorescence cuvette of 1 cm path length (Hellma). Wavenumbers were calibrated with respect to the silicon scattering line at $520(1)\text{ cm}^{-1}$ of an internal standard. Elemental analyzes were performed on a Flash EA 1112 (Thermo Scientific) CHNS analyzer at the "Plateforme d'Analyses Chimiques et de Synthèse Moléculaire de l'Université de Bourgogne - Pôle Chimie Moléculaire" (PACSMUB), the technological platform for chemical analysis and molecular synthesis (<http://www.wpcm.fr>). Thermogravimetric analyzes (TGA) were carried out on a Netzsch STA 409 PC Luxx thermoanalyzer using alumina crucibles. Samples purged in an nitrogen (30 mL/min)/dioxygen (10 mL/min) stream were heated up to $1000\text{ }^\circ\text{C}$ with a heating rate of $5\text{ }^\circ\text{C}/\text{min}$. Data were corrected for buoyancy effects.

Synthesis of $[\text{Fe}(\text{NMA})_3]$. $\text{Fe}(\text{acac})_3$ (287 mg, 0.813 mmol) dissolved in 8 mL of CH_3OH was added to solution of NMAH (250 mg, 2.806 mmol) in CH_3OH (15 mL) at room

temperature. The resulting reaction mixture turned immediately red-brown. After stirring it for 2 h, the solvent was removed under vacuum and the solid residue dissolved in 2 mL of CH₂Cl₂. The resulting solution was topped with 10 mL of cyclohexane without mixing and left at room temperature to allow slow diffusion and evaporation. After 1 d, the remaining supernatant solution (about half of the initial volume) was discarded and X-ray quality crystals were collected for subsequent diffraction studies (*vide infra*). The remaining crystalline solid was washed with a mixture of 2 mL of CH₂Cl₂ and 15 mL of cyclohexane, and finally dried under vacuum for 5 h. Yield: 250 mg (0.755 mmol, 93%) of a red-brown solid. IR (ATR, cm⁻¹): $\tilde{\nu}$ = 3460 (br, $\nu(\text{O-H})$, w), 2941 (w), 1658 (w), 1592 (s), 1472 (s), 1422 (s), 1369 (m), 1229 (w), 1167 (m), 1029 (w), 968 (s), 753 (s), 625 (s), 601 (m), 546 (s), 496 (s). Anal. calcd. (%) for C₉H₁₈FeN₃O₆·0.6H₂O (330.91 g/mol): C 32.67, H 5.85, N 12.70; found: C 32.59, H 5.72, N 12.74. The water content is in good agreement with TGA measurements: Δm = 2.3% at 80 °C (loss of 0.41 water molecule/complex), Δm = 74.2% at 370 °C (Δm = 75.7% calcd. for residual Fe₂O₃).

Synthesis of [UO₂(NMA)₂(H₂O)]. To an aqueous solution (5 mL) of NMAH (100 mg, 1.122 mmol) at pH 4.9 was added in one portion 141 mg (0.281 mmol) of [UO₂(NO₃)₂(H₂O)₂] \cdot 4H₂O. After dissolution, the pH dropped to 1.7 and the reaction mixture became orange, indicating complex formation. The pH was then adjusted to 5.1 with ca. 5 mL of a 0.1 M N(CH₃)₄OH solution. Red-orange crystals deposited upon partial slow evaporation of the mother liquor. X-ray diffraction studies evidenced unambiguously the [UO₂(NMA)₂(H₂O)] formula.³ The remaining crystalline solid was recovered by filtration, washed with a minimum amount of water, and dried under vacuum. Yield: 80 mg (0.172 mmol, 61%). IR (ATR, cm⁻¹): $\tilde{\nu}$ = 2938 (v br, w), 1718 (w), 1597 (s), 1475 (s), 1419 (s), 1374 (m), 1217 (m), 1164 (s), 1034 (w), 972 (m), 896 ($\nu_{\text{as}}(\text{U=O})$, s), 830 ($\nu_{\text{s}}(\text{U=O})$, w), 752 (s), 612 (s), 595 (m), 486 (s). Raman (cm⁻¹): $\tilde{\nu}$ = 2939, 1622, 1603, 828 ($\nu_{\text{s}}(\text{U=O})$, vs), 757,

221. Anal. calcd. (%) for $C_6H_{14}N_2O_7U$ (464.21 g/mol): C 15.52, H 3.04, N 6.03; found: C 15.61, H 3.06, N 6.09.

Synthesis of $[U^{18}O_2(NMA)_2(H_2O)]$. To an aqueous solution (3 mL) of NMAH (7 mg, 0.0785 mmol) was added 0.5 mL of a 0.1 M $N(CH_3)_4OH$ solution followed by 0.1 mL (0.02 mmol) of an ~ 0.2 M $U^{18}O_2(NO_3)_2$ solution acidified with HNO_3 (~ 0.09 M). The reaction mixture became orange and the pH was adjusted to 5.3 with ca. 0.1 mL of a 0.1 M $N(CH_3)_4OH$ solution. The solution was then evaporated to dryness under vacuum and analyzed without further purification. IR (ATR, cm^{-1}): $\tilde{\nu} = 2939$ (v br, w), 1599 (m), 1491 (s), 1415 (w), 1331 (br, s), 1215 (w), 1162 (w), 1033 (w), 968 (w), 947 (s), 889 (w), 877 (w), 850 ($\nu_{as}(U=^{18}O)$, s), 832 (w), 752 (m), 612 (m), 482 (m), 459 (w). Raman (cm^{-1}): $\tilde{\nu} = (\nu_s(U=O), \nu_s)$. Isotopic exchange on the uranyl center in the bischelated complex was ascertained by the bathochromic shift experienced both by the Raman and IR active symmetric and antisymmetric U=O stretching modes, respectively. The wavenumbers found for the labeled complex, $\nu_s(U=O) = 785$ and $\nu_{as}(U=O) = 850$ cm^{-1} , are in perfect agreement with the values predicted by the Hooke's law $\nu(U=^{18}O) = \nu(U=^{16}O) \times (\mu_{U=^{16}O}/\mu_{U=^{18}O})^{1/2} = 0.947$, where μ designates the reduced mass of the harmonic vibrator ($\mu = M_U M_O / M_U + M_O$).

Crystallography. Clear dark-red plate-shaped single crystals of $[Fe(NMA)_3] \cdot H_2O$ suitable for X-ray crystallography were obtained by slow diffusion of cyclohexane (10 mL) into a dichloromethane solution (2 mL) of the isolated complex. A specimen with dimensions of $0.15 \times 0.12 \times 0.02$ mm^3 was selected and mounted on a MITIGEN holder oil on a Bruker D8 VENTURE diffractometer equipped with an Oxford Cryosystems low-temperature device operating at $T = 100(2)$ K. Data were measured using ϕ and ω scans of 1.00° per frame for 120.00 s using the Cu K_α radiation from a sealed X-ray tube. Cell parameter refinement and data reduction were performed using the SAINT software, which corrects for Lorentz polarization.²⁹ The structure was solved in the space group $P2_1/n$ by direct methods using the

ShelXT software³⁰ and then refined by full-matrix least-squares on F^2 using ShelXL (release 2014/7),³¹ both routines being implemented in the Olex2 environment.³² All non-hydrogen atoms were refined anisotropically. Hydrogen atoms were placed at calculated positions and refined using a riding model.

Crystal Data for [Fe(NMA)₃]-H₂O. C₉H₂₀FeN₃O₇, $M_r = 338.13$ g/mol, monoclinic space group $P2_1/n$ (No. 14), $a = 10.4087(6)$ Å, $b = 10.4063(6)$ Å, $c = 27.484(2)$ Å, $\beta = 91.156(3)^\circ$, $V = 2976.3(3)$ Å³, $Z = 8$, $Z' = 2$, $\rho_{\text{calcd}} = 1.509$ g/cm³, $T = 100(2)$ K, $\mu(\text{Cu K}\alpha) = 8.458$ mm⁻¹ ($\lambda = 1.54184$ Å), 30590 reflections measured ($6.432^\circ \leq 2\theta \leq 133.37^\circ$), 5184 unique ($R_{\text{int}} = 0.0544$, $R_{\text{sigma}} = 0.0369$), 4460 used with $I > 2\sigma(I)$, 370 parameters and 16 restraints. Final $R_1 = 0.0375$ ($I > 2\sigma(I)$), $wR_2 = 0.1006$ (all data), min./max. residual electron density = $-0.282/0.648$ e/Å³. Some disorder (50%) was found in the crystal structure and some geometric parameters of disordered components in each group were restrained by using EADP constraints or RIGU restraints. See the Supporting Information for more details.

Mass Spectrometry Measurements. Mass spectrometry experiments were conducted with a Finnigan LCQ instrument equipped with an electrospray ionization source operated in a positive charge mode.³³ Methanolic solutions of the complexes were introduced to the electrospray ionization source through a fused-silica capillary using a syringe-pump. The operating conditions were set as following: spray voltage to 4.55 kV, capillary voltage to 0 V, and the temperature of the capillary to 150 °C. Collision-induced dissociation of mass-selected ions was achieved by excitation of the ions at their secular frequency and collision with the helium buffer gas.

Alternatively, high-resolution (+)-ESI-MS spectra of ¹⁸O enriched uranyl samples dissolved in methanol were acquired at the PACSMUB platform on a LTQ OrbitrapXL (Thermo Scientific) spectrometer equipped with a Ion Max source and HESI-II probe. Solutions were injected with a syringe pump at a flow rate of 5 $\mu\text{L}/\text{min}$. Spectra were

collected using the following settings: heater temperature: 50 °C, spray voltage: +4 kV, capillary temperature: 275 °C, capillary voltage: 0 V, tube lens: 20 V, sheath gas pressure: 10 psi. The resolution was set to 60 000 at $m/z = 200$ amu. CID experiments were carried out with helium as collision gas. The analyzed ion was selected with an isolation width of $m/z = 1$ amu. The normalized collision energy, as defined by the constructor, was varied step by step between 0 and 18%. The other instrumental parameters were set to 0.25 for the activation Q (a parameter that defines the frequency of the applied radiofrequency potential) and 30 ms for the activation time.

Infrared multiphoton dissociation (IRMPD) spectra were collected with a Bruker Esquire 3000 ion trap mass spectrometer. The IR photons were provided by free electron laser CLIO (Centre Laser Infrarouge Orsay, Orsay, France).³⁴ The ions were generated in the same way as above, mass selected, and stored in the ion trap. The mass-selected ions were irradiated by several laser macropulses that induced a fragmentation (the wavenumber power dependence is shown in Figure S14; irradiation time was 150 ms). The dependence of the fragmentation yield on the photon wavenumber provides the experimental IRMPD spectrum with a resolution of 15–20 cm^{-1} .³⁵

DFT Calculations. Theoretical calculations were conducted using DFT methods with Gaussian 09 package rev. D.³⁶ Specifically, we used the unrestricted B3LYP method,³⁷ comprised of Becke exchange (B3)³⁸ and Lee, Yang and Parr's gradient-corrected correlation functional (LYP).³⁹ Structures were optimized using B3LYP functional and cc-pVTZ basis set (for organic atoms H, C, N and O) and Stuttgart pseudo-potential (SDD) basis set (for U and Fe). For each optimized structure, the frequency calculation was performed in order to validate the minimum on the potential energy surface, calculate the zero-point energy (ZPE), and obtain the infrared spectrum. The predicted gas spectra were broadened using a Gaussian function with a full width at half-maximum of 10 cm^{-1} . For all theoretical spectra, the scaling

factor was chosen in order to obtain the best agreement with the experimental data. Scaling factors of 0.99 and 0.985 were used for the iron and uranium complexes of NMA⁻, respectively. A factor of 0.98 was applied for the free ligand. In order to gain more insights about the bonding character, we have used Natural Bond Orbitals (NBO) analysis, as implemented in Gaussian 09, i.e. NBO 3.0.⁴⁰

ASSOCIATED CONTENT

Supporting Information

The Supporting Information is available free of charge on the ACS Publications website at DOI: 10.1021/acs.inorgchem.XXX.

Crystallographic data for [Fe(NMA)₃]·H₂O; statistics on bond distances for iron hydroxamate complexes; TGA, FTIR, and ESI-MS data for [Fe(NMA)₃]·0.6H₂O; IRMPD data for [Fe₂(NMA)₅]⁺; FTIR and ESI-MS data for [UO₂(NMA)₂(H₂O)]; CID spectra for selected ions generated from [UO₂(NMA)₂(H₂O)] and [U¹⁸O₂(NMA)₂(H₂O)]; laser power during IRMPD measurements; detailed assignment of the IR spectra of NMAH, NMA⁻, **Fe_{mono1}**, **Fe_{mono2}**, **Fe_{di1}**, and **U₁**; Mulliken charge distribution for NMAH, NMA⁻, **Fe_{mono2}**; DFT-calculated bond distances for NMAH, NMA⁻, **Fe_{mono2}**, **Fe_{di1}**, and **U₁**; NBO analysis of **Fe_{mono2}**, **U₁**, and **Fe_{di1}** (pdf).

Accession Codes

CCDC-1538337 contains the supplementary crystallographic data for this paper. These data can be obtained free of charge via www.ccdc.cam.ac.uk/data_request/cif, or by e-mailing

data_request@ccdc.cam.ac.uk, or by contacting The Cambridge Crystallographic Data Centre, 12 Union Road, Cambridge CB2 1EZ, U.K.; fax: +44 1223 336033.

AUTHOR INFORMATION

Corresponding Authors

* E-mail: roithova@natur.cuni.cz.

* E-mail: michel.meyer@u-bourgogne.fr.

ORCID

Jana Roithova: 0000-0001-5144-0688

Michel Meyer: 0000-0003-2295-7826

Stéphane Brandès: 0000-0001-6923-1630

Notes

The authors declare no competing financial interest.

ACKNOWLEDGEMENTS

The Czech Science Foundation (14-20077S), the Centre National de la Recherche Scientifique (CNRS), the Conseil Régional de Bourgogne through the "Plan d'Actions Régional pour l'Innovation" (program PARI II CDEA), the European Regional Development Fund (FEDER), the French-Czech exchange program "Partenariat Hubert Curien (PHC) Barrande", and the program "Défi NEEDS Environnement" (project ACTISOL) are gratefully acknowledged for their financial support. Measurements at CLIO were performed owing to

the funding from the European Union's Seventh Framework Program (FP7/2007-2013) under the grant agreement No. 226716. The CLIO staff, particularly Vincent Steinmetz, is acknowledged for their help and assistance.

REFERENCES

- (1) Lossen, H. Uber die Oxalohydroxamsäure. *Justus Liebigs Ann. Chem.* **1869**, *150*, 314-322.
- (2) (a) Kakkar, R.; Grover, R.; Chadha, P. Conformational behavior of some hydroxamic acids. *Org. Biomol. Chem.* **2003**, *1*, 2200-2206. (b) Gupta, S. P.; Sharma, A. The Chemistry of Hydroxamic Acids. In *Hydroxamic Acids*; Gupta, S. P., Ed.; Springer: Berlin, 2013, p 1-17.
- (3) Brandès, S.; Sornosa-Ten, A.; Rousselin, Y.; Lagrelette, M.; Stern, C.; Moncomble, A.; Cornard, J.-P.; Meyer, M. Conformational and structural studies of *N*-methylacetohydroxamic acid and of its mono- and bis-chelated uranium(VI) complexes. *J. Inorg. Biochem.* **2015**, *151*, 164-175.
- (4) Miethke, M.; Marahiel, M. A. Siderophore-based iron acquisition and pathogen control. *Microbiol. Mol. Biol. Rev.* **2007**, *71*, 413-451.
- (5) (a) Brown, D. A.; McKeith, D.; Glass, W. K. The infrared spectra of monohydroxamic acid complexes of copper, iron and nickel. *Inorg. Chim. Acta* **1979**, *35*, 57-60. (b) Codd, R. Traversing the coordination chemistry and chemical biology of hydroxamic acids. *Coord. Chem. Rev.* **2008**, *252*, 1387-1408. (c) Ducháčková, L.; Roithová, J. The interaction of zinc(II) and hydroxamic acids and a metal-triggered lossen rearrangement. *Chem.–Eur. J.* **2009**, *15*, 13399-13405. (d) Jewula, P.; Berthet, J.-C.; Chambron, J.-C.; Rousselin, Y.; Thuéry, P.; Meyer, M. Synthesis and Structural Study of Tetravalent (Zr^{4+} , Hf^{4+} , Ce^{4+} , Th^{4+} , U^{4+}) Metal Complexes with Cyclic Hydroxamic acids. *Eur. J. Inorg. Chem.* **2015**, 1529-1541. (e) Springer, S. D.; Butler, A. Microbial ligand coordination: Consideration of biological significance. *Coord. Chem. Rev.* **2016**, *306*, 628-635.
- (6) Ahmed, E.; Holmström, S. J. M. Siderophores in environmental research: Roles and

- applications. *Microb. Biotechnol.* **2014**, *7*, 196-208.
- (7) Harris, W. R.; Carrano, C. J.; Raymond, K. N. Coordination chemistry of microbial iron transport compounds. 16. Isolation, characterization, and formation constants of ferric aerobactin. *J. Am. Chem. Soc.* **1979**, *101*, 2722-2727.
- (8) Hoshino, Y.; Okuno, M.; Kawamura, E.; Honda, K.; Inoue, S. Base-mediated rearrangement of free aromatic hydroxamic acids (ArCO-NHOH) to anilines. *Chem. Commun.* **2009**, 2281-2283.
- (9) Jašíková, L.; Hanikýřová, E.; Škríba, A.; Jašík, J.; Roithová, J. Metal-assisted lossen rearrangement. *J. Org. Chem.* **2012**, *77*, 2829-2836.
- (10) (a) Raymond, K. N.; Freeman, G. E.; Kappel, M. J. Actinide-specific complexing agents: Their structural and solution chemistry. *Inorg. Chim. Acta* **1984**, *94*, 193-204. (b) Ruggiero, C. E.; Matonic, J. H.; Reilly, S. D.; Neu, M. P. Dissolution of Plutonium(IV) Hydroxide by Desferrioxamine Siderophores and Simple Organic Chelators. *Inorg. Chem.* **2002**, *41*, 3593-3595. (c) Gorden, A. E. V.; Xu, J.; Raymond, K. N.; Durbin, P. Rational Design of Sequestering Agents for Plutonium and Other Actinides. *Chem. Rev.* **2003**, *103*, 4207-4282. (d) Boukhalfa, H.; Reilly, S. D.; Neu, M. P. Complexation of Pu(IV) with the Natural Siderophore Desferrioxamine B and the Redox Properties of Pu(IV)(siderophore) Complexes. *Inorg. Chem.* **2007**, *46*, 1018-1026. (e) Neu, M. P.; Matonic, J. H.; Ruggiero, C. E.; Scott, B. L. Structural Characterization of a Plutonium(IV) Siderophore Complex: Single-Crystal Structure of Pu-Desferrioxamine E. *Angew. Chem., Int. Ed.* **2000**, *39*, 1442-1444. (f) Xu, C.; Zhang, S.; Kaplan, D. I.; Ho, Y.-F.; Schwehr, K. A.; Roberts, K. A.; Chen, H.; DiDonato, N.; Athon, M.; Hatcher, P. G.; Santschi, P. H. Evidence for Hydroxamate Siderophores and Other N-Containing Organic Compounds Controlling ^{239,240}Pu Immobilization and Remobilization in a Wetland Sediment. *Environ. Sci. Technol.* **2015**, *49*, 11458-11467.

- (11) (a) Matys Grygar, T.; Elznicová, J.; Bábek, O.; Hošek, M.; Engel, Z.; Kiss, T. Obtaining isochrones from pollution signals in a fluvial sediment record: A case study in a uranium-polluted floodplain of the Ploučnice River, Czech Republic. *Appl. Geochem.* **2014**, *48*, 1-15. (b) Dias da Cunha, K. M.; Henderson, H.; Thomson, B. M.; Hecht, A. A. Ground water contamination with ^{238}U , ^{234}U , ^{235}U , ^{226}Ra and ^{210}Pb from past uranium mining: Cove wash, Arizona. *Environ. Geochem. Health* **2014**, *36*, 477-487.
- (12) (a) Mullen, L.; Gong, C.; Czerwinski, K. Complexation of uranium(VI) with the siderophore desferrioxamine B. *J. Radioanal. Nucl. Chem.* **2007**, *273*, 683-688. (b) Tkac, P.; Matteson, B.; Brusio, J.; Paulenova, A. Complexation of uranium(VI) with acetohydroxamic acid. *J. Radioanal. Nucl. Chem.* **2008**, *277*, 31-36.
- (13) Kurzak, B.; Kozłowski, H.; Farkas, E. Hydroxamic and aminohydroxamic acids and their complexes with metal ions. *Coord. Chem. Rev.* **1992**, *114*, 169-200.
- (14) Groenewold, G. S.; Van Stipdonk, M. J.; Gresham, G. L.; Chien, W.; Bulleigh, K.; Howard, A. Collision-induced dissociation tandem mass spectrometry of desferrioxamine siderophore complexes from electrospray ionization of UO_2^{2+} , Fe^{3+} and Ca^{2+} solutions. *J. Mass Spectrom.* **2004**, *39*, 752-761.
- (15) Kepert, D. L. *Inorganic Stereochemistry*; Springer Verlag: Heidelberg, Germany, 1982; Vol. 6.
- (16) (a) MacAleese, L.; Maître, P. Infrared spectroscopy of organometallic ions in the gas phase: From model to real world complexes. *Mass Spectrom. Rev.* **2007**, *26*, 583-605 and references therein. (b) Polfer, N. C.; Oomens, J. Vibrational spectroscopy of bare and solvated ionic complexes of biological relevance. *Mass Spectrom. Rev.* **2009**, *28*, 468-494. (c) Roithová, J. Characterization of reaction intermediates by ion spectroscopy. *Chem. Soc. Rev.* **2012**, *41*, 547-559.
- (17) Silver, M. A.; Dorfner, W. L.; Cary, S. K.; Cross, J. N.; Lin, J.; Schelter, E. J.; Albrecht-

- Schmitt, T. E. Why Is Uranyl Formohydroxamate Red? *Inorg. Chem.* **2015**, *54*, 5280-5284.
- (18) Politzer, P.; Murray, J. S. Some Intrinsic Features of Hydroxylamines, Oximes and Hydroxamic Acids: Integration of Theory and Experiment. In *The Chemistry of Hydroxylamines, Oximes and Hydroxamic Acids*; Rappoport, Z., Liebman, J. F., Eds.; John Wiley & Sons: Chichester, UK, 2008, p 1-27.
- (19) Dhungana, S.; White, P. S.; Crumbliss, A. L. Crystal structure of ferrioxamine B: a comparative analysis and implications for molecular recognition. *J. Biol. Inorg. Chem.* **2001**, *6*, 810-818.
- (20) Shannon, R. D. Revised Effective Ionic Radii and Systematic Studies of Interatomic Distances in Halides and Chalcogenides. *Acta Crystallogr., Sect. A* **1976**, *32*, 751-767.
- (21) Edwards, D. C.; Nielsen, S. B.; Jarzęcki, A. A.; Spiro, T. G.; Myneni, S. C. B. Experimental and theoretical vibrational spectroscopy studies of acetohydroxamic acid and desferrioxamine B in aqueous solution: Effects of pH and iron complexation. *Geochim. Cosmochim. Acta* **2005**, *69*, 3237-3248.
- (22) Wu, Q.-Y.; Zhai, F.-W.; Liu, Y.; Yuan, L.-Y.; Chai, Z.-F.; Shi, W.-Q. Interactions between uranium(VI) and phosphopeptide: experimental and theoretical investigations. *Dalton Trans.* **2016**, *45*, 14988-14997.
- (23) Barros, N.; Maynau, D.; Maron, L.; Eisenstein, O.; Zi, G.; Andersen, R. A. Single but Stronger UO, Double but Weaker UNMe Bonds: The Tale Told by Cp₂UO and Cp₂UNR. *Organometallics* **2007**, *26*, 5059-5065.
- (24) Domagal-Goldman, S. D.; Paul, K. W.; Sparks, D. L.; Kubicki, J. D. Quantum chemical study of the Fe(III)-desferrioxamine B siderophore complex-Electronic structure, vibrational frequencies, and equilibrium Fe-isotope fractionation. *Geochim. Cosmochim. Acta* **2009**, *73*, 1-12.

- (25) Lemire, J. A.; Harrison, J. J.; Turner, R. J. Antimicrobial activity of metals: mechanisms, molecular targets and applications. *Nat. Rev. Micro.* **2013**, *11*, 371-384.
- (26) (a) Gong, Y.; Vallet, V.; del Carmen Michelini, M.; Rios, D.; Gibson, J. K. Activation of Gas-Phase Uranyl: From an Oxo to a Nitrido Complex. *J. Phys. Chem. A* **2014**, *118*, 325-330. (b) Van Stipdonk, M. J.; Michelini, M. d. C.; Plaviak, A.; Martin, D.; Gibson, J. K. Formation of Bare UO_2^{2+} and NUO^+ by Fragmentation of Gas-Phase Uranyl–Acetonitrile Complexes. *J. Phys. Chem. A* **2014**, *118*, 7838-7846. (c) Gong, Y.; de Jong, W. A.; Gibson, J. K. Gas Phase Uranyl Activation: Formation of a Uranium Nitrosyl Complex from Uranyl Azide. *J. Am. Chem. Soc.* **2015**, *137*, 5911-5915.
- (27) Abergel, R. J.; de Jong, W. A.; Deblonde, G. J. P.; Dau, P. D.; Captain, I.; Eaton, T. M.; Jian, J.; van Stipdonk, M. J.; Martens, J.; Berden, G.; Oomens, J.; Gibson, J. K. Cleaving Off Uranyl Oxygens through Chelation: A Mechanistic Study in the Gas Phase. *Inorg. Chem.* **2017**, *56*, 12930-12937.
- (28) Szabó, Z.; Grenthe, I. Reactivity of the “yl”-Bond in Uranyl(VI) Complexes. 1. Rates and Mechanisms for the Exchange between the trans-dioxo Oxygen Atoms in $(\text{UO}_2)_2(\text{OH})_2^{2+}$ and Mononuclear $\text{UO}_2(\text{OH})_n^{2-n}$ Complexes with Solvent Water. *Inorg. Chem.* **2007**, *46*, 9372-9378.
- (29) SAINT: Area-Detector Integration Software, v. 8.37A; Bruker: Madison, Wisconsin, USA, 2013.
- (30) Sheldrick, G. M. SHELXT - Integrated space-group and crystal-structure determination. *Acta Crystallogr., Sect. A* **2015**, *71*, 3-8.
- (31) Sheldrick, G. Crystal structure refinement with SHELXL. *Acta Crystallogr., Sect. C* **2015**, *71*, 3-8.
- (32) Dolomanov, O. V.; Bourhis, L. J.; Gildea, R. J.; Howard, J. A. K.; Puschmann, H. OLEX2: a complete structure solution, refinement and analysis program. *J. Appl. Crystallogr.* **2009**,

- 42, 339-341.
- (33) (a) Škríba, A.; Schulz, J.; Roithová, J. Monitoring of Reaction Intermediates in the Gas Phase: Ruthenium-Catalyzed C–C Coupling. *Organometallics* **2014**, *33*, 6868-6878. (b) Schulz, J.; Jašíková, L.; Škríba, A.; Roithová, J. Role of Gold(I) α -Oxo Carbenes in the Oxidation Reactions of Alkynes Catalyzed by Gold(I) Complexes. *J. Am. Chem. Soc.* **2014**, *136*, 11513-11523. (c) Gray, A.; Tsybizova, A.; Roithova, J. Carboxylate-assisted C-H activation of phenylpyridines with copper, palladium and ruthenium: a mass spectrometry and DFT study. *Chem. Sci.* **2015**, *6*, 5544-5553.
- (34) Ortega, J. M.; Glotin, F.; Prazeres, R. Extension in far-infrared of the CLIO free-electron laser. *Infrared Phys. Technol.* **2006**, *49*, 133-138.
- (35) (a) Aleese, L. M.; Simon, A.; McMahon, T. B.; Ortega, J.-M.; Scuderi, D.; Lemaire, J.; Maître, P. Mid-IR spectroscopy of protonated leucine methyl ester performed with an FTICR or a Paul type ion-trap. *Int. J. Mass Spectrom.* **2006**, *249-250*, 14-20. (b) Paizs, B.; Bythell, B. J.; Maître, P. Rearrangement Pathways of the α_4 Ion of Protonated YGGFL Characterized by IR Spectroscopy and Modeling. *J. Am. Soc. Mass Spectrom.* **2012**, *23*, 664-675.
- (36) Frisch, M. J.; Trucks, G. W.; Schlegel, H. B.; Scuseria, G. E.; Robb, M. A.; Cheeseman, J. R.; Scalmani, G.; Barone, V.; Mennucci, B.; Petersson, G. A.; Nakatsuji, H.; Caricato, M.; Li, X.; Hratchian, H. P.; Izmaylov, A. F.; Bloino, J.; Zheng, G.; Sonnenberg, J. L.; Hada, M.; Ehara, M.; Toyota, K.; Fukuda, R.; Hasegawa, J.; Ishida, M.; Nakajima, T.; Honda, Y.; Kitao, O.; Nakai, H.; Vreven, T.; Montgomery, J. A.; Peralta, J. E.; Ogliaro, F.; Bearpark, M.; Heyd, J. J.; Brothers, E.; Kudín, K. N.; Staroverov, V. N.; Kobayashi, R.; Normand, J.; Raghavachari, K.; Rendell, A.; Burant, J. C.; Iyengar, S. S.; Tomasi, J.; Cossi, M.; Rega, N.; Millam, J. M.; Klene, M.; Knox, J. E.; Cross, J. B.; Bakken, V.; Adamo, C.; Jaramillo, J.; Gomperts, R.; Stratmann, R. E.; Yazyev, O.; Austin, A. J.; Cammi, R.;

- Pomelli, C.; Ochterski, J. W.; Martin, R. L.; Morokuma, K.; Zakrzewski, V. G.; Voth, G. A.; Salvador, P.; Dannenberg, J. J.; Dapprich, S.; Daniels, A. D.; Farkas, Ö.; Foresman, J. B.; Ortiz, J. V.; Cioslowski, J.; Fox, D. J. Gaussian 09 revision 01, Gaussian Inc.: Wallingford CT, 2016.
- (37) Stephens, P.; Devlin, F. J.; Chabalowski, C. F.; Frisch, M. J. Ab-Initio Calculation of Vibrational Absorption and Circular-Dichroism Spectra Using Density-Functional Force-Fields. *J. Phys. Chem.* **1994**, *98*, 11623-11627.
- (38) Becke, A. D. Density-functional thermochemistry. III. The role of exact exchange. *J. Chem. Phys.* **1993**, *98*, 5648.
- (39) Lee, C.; Yang, W.; Parr, R. G. Development of the Colle-Salvetti correlation-energy formula into a functional of the electron density. *Phys. Rev. B* **1988**, *37*, 785-789.
- (40) (a) Reed, A. E.; Weinhold, F. Natural bond orbital analysis of near - Hartree–Fock water dimer. *J. Chem. Phys.* **1983**, *78*, 4066-4073. (b) Reed, A. E.; Weinstock, R. B.; Weinhold, F. Natural population analysis. *J. Chem. Phys.* **1985**, *83*, 735-746. (c) Carpenter, J. E.; Weinhold, F. Analysis of the geometry of the hydroxymethyl radical by the “different hybrids for different spins” natural bond orbital procedure. *J. Mol. Struct.: THEOCHEM* **1988**, *169*, 41-62. (d) Foster, J. P.; Weinhold, F. Natural hybrid orbitals. *J. Am. Chem. Soc.* **1980**, *102*, 7211-7218.

Table of Contents

Highly polarized covalent bonds of similar nature have been evidenced by DFT calculations and IRMPD spectroscopy for N-methylacetohydroxamate (NMA⁻) complexes of Fe³⁺ and UO₂²⁺, albeit with slightly stronger ionic character for the later. Upon collisional activation, the gas phase cation [UO₂(NMA)(NMAH)₂]⁺ easily eliminates a water molecule through abstraction of one uranyl oxo ligand. This unusual dissociation pattern highlights a specific reactivity of the "yl" oxygen atom bound to uranium(VI).

